Nanoscale Horizons

ROYAL SOCIETY OF CHEMISTRY

COMMUNICATION

View Article Online
View Journal | View Issue

Check for updates

Cite this: *Nanoscale Horiz.*, 2026, **11**, 1081

Received 22nd October 2025,
Accepted 22nd December 2025

DOI: 10.1039/d5nh00708a

rsc.li/nanoscale-horizons

In vivo tracking of CAR-T cells in tumors *via* nanobubble-based contrast enhanced ultrasound

Dorian Durig, [a] Jude Franklin, [a] Reshani Perera, [b] Zachary Jackson, [c] Smitha Hosahalli Vasanna, [g] Michael C. Kolios, [ef] David N. Wald *[cd] and Agata A. Exner *[ab]

CAR-T cell therapy has led to remarkable advances in the outcomes of patients with acute lymphoblastic leukemia (ALL), B cell lymphomas, and multiple myeloma. Given these successes in hematologic malignancies, extensive efforts are now focused on developing CAR-T cell therapies to treat solid tumors. The treatment of solid tumors poses significant hurdles with cell trafficking necessary to achieve efficacy and minimize off-tumor side effects. The development of simple, safe and inexpensive modalities for tracking CAR-T cell distribution in clinical use *in vivo* could provide critical insights to facilitate the development of improved CAR-T products for solid tumors. Here, we demonstrate a strategy to monitor CAR-T cells *in vivo* using ultrasound imaging of nanobubble (NB) labeled cells. NBs are ultrasound contrast agents composed of a lipid shell and a C_4F_{10} gas core that can be efficiently internalized into cells. This approach enables us to image the CAR-T cells using nonlinear contrast-enhanced ultrasound (CEUS). Utilizing this method, we found that CAR-T cells can be visualized after injection into both tumor-bearing and non-tumor bearing mice. In summary, our ultrasound-based tracking approach can effectively monitor the trafficking of CAR-T cells *in vivo*, offering a valuable new strategy that can further enable the development of new CAR-T products and strategies to modulate cell trafficking.

New concepts

This study demonstrates a novel concept in nanomedicine: the feasibility of non-invasively tracking CAR-T cells using nanosized ultrasound contrast agents. This innovative approach addresses critical challenges in understanding CAR-T cell infiltration and localization within solid tumor environments. Unlike existing methods for non-invasive CAR-T cell tracking, which are often limited by high costs, restricted accessibility, reduced cell viability, or reliance on radiation exposure, our method leverages nanobubbles combined with ultrasound to offer a cost-effective, safe, and widely accessible alternative. By utilizing nanobubble internalization in CAR-T cells, this research establishes an innovative method for ultrasound-based immune cell tracking. It offers valuable insights into the potential of nanotechnology to improve CAR-T cell therapy, particularly in overcoming the challenges associated with treating solid tumors. These findings contribute to the field of materials science by showcasing how nanoscale engineering can enable practical and clinically relevant solutions in immune cell tracking and therapy.

Introduction

Chimeric antigen receptor T cell (CAR-T) therapy is an advanced form of adoptive cell therapy (ACT) that has significantly impacted the field of immunotherapy. CAR-T cell therapy uses patient-specific T cells to create several FDA-approved products to treat B-cell malignancies and multiple myeloma.[1,2] The manufacturing process involves the genetic engineering of the patient's T cells to express a chimeric antigen receptor directed towards a target antigen expressed on tumor cells such as CD19, which is expressed specifically on malignant and normal B cells. The genetically modified T cells are intravenously infused into the patient where it is hoped that they will traffic to the tumor, expand, and kill the tumor cells.

Despite notable achievements in hematological malignancies, the success of CAR-T therapy has not been reproduced in treating solid tumors.[3] The limited success is hypothesized to be attributed to multiple factors, including an immunosuppressive tumor microenvironment, on-target off-tumor toxicity, T cell exhaustion, tumor heterogeneity, poor trafficking to the tumors, and lack of CAR-T cell persistence.[4] To

[a] *Department of Biomedical Engineering, Case Western Reserve University, Cleveland, Ohio 44106, USA. E-mail: aas11@case.edu*
[b] *Department of Radiology, Case Western Reserve University, Cleveland, Ohio 44106, USA*
[c] *Department of Pathology, Case Western Reserve University, Cleveland, Ohio 44106, USA*
[d] *Department of Pathology, University Hospitals Cleveland Medical Center, Cleveland, Ohio 44106, USA. E-mail: dnw@case.edu*
[e] *Department of Physics Toronto Metropolitan University, Toronto, Ontario, M5B 2K3, Canada*
[f] *Institute for Biomedical Engineering, Science and Technology (iBEST), a partnership between St. Michael's Hospital, a site of Unity Health Toronto and Toronto Metropolitan University*
[g] *Department of Pediatrics, University Hospitals Cleveland Medical Center, Cleveland, Ohio 44106, USA*

understand the factors contributing to the limited success of CAR-T cells in treating tumors, and to better finetune dosage parameters while mitigating side effects, such as neurotoxicity and cytokine release syndrome, the biodistribution and trafficking of the cells to the target after infusion need to be studied.[5]

Currently, clinically available methods are inadequate for assessing the real-time trafficking patterns of CAR-T cells in organs and tumors, which is essential for evaluating treatment efficacy and adjusting strategies accordingly. The standard practice for monitoring cellular kinetics and patient responses to immunotherapy involves intermittent blood draws, which provides valuable information such as white blood cell counts and the presence of CAR DNA.[6] However, these tests fail to reveal the biodistribution and movement of CAR-T cells within the body. Real-time tracking of immune treatments would allow for a more comprehensive understanding of how CAR-T cells engage with the tumor microenvironment, providing timely insights that can improve therapeutic outcomes.

The benefits of tracking CAR-T cells *via* imaging have recently been recognized, leading to the adoption of various techniques that utilize modalities such as MRI, PET, and optical imaging, each providing unique information that surpasses the periodic blood draws used in the clinic.[7–12] These approaches, however, also have disadvantages and limitations: MRI suffers from low temporal resolution and high costs, PET is associated with radiation exposure and limited spatial resolution, while optical imaging has shallow penetration depth and is restricted to superficial tissues.[13,14] Although each technique offers valuable information, no single method has been established as the definitive standard for monitoring the trafficking and distribution of cells. To provide an alternative strategy for tracking CAR-T cells *in vivo*, we investigate using contrast-enhanced ultrasound (CEUS).

Ultrasound (US) imaging is a non-ionizing modality that is widely used and accessible at a low cost. It offers deep penetration and high spatial and temporal resolution, making it extensively used for ultrasound-guided procedures and examinations, including guidance of cell transplant injections.[15–18] However, even in these applications, the transplanted cells can be difficult to differentiate from surrounding soft tissue, mirroring the challenges faced in identifying immune cells following immunotherapy treatment. As a result, US contrast agents (UCAs) have become a promising tool for enhancing cell visibility by labeling cells, thereby increasing their contrast relative to surrounding tissue.[18–21]

UCAs are made up of lipids, proteins, or polymers that form a shell around a gas core, creating a bubble.[22] Microbubbles (MBs), which are commercially available UCAs, range in size from approximately 1 to 8 μm and are primarily used to enhance vascular imaging due to their confinement within the vasculature.[22,23] However, nanosized contrast agents, such as nanobubbles (NBs), have emerged as an alternative to MBs due to their smaller size of approximately 100–600 nm in diameter.[15] This smaller size allows NBs to move beyond the vasculature, making them a more promising UCA for labeling cells expected to extravasate and infiltrate tissue. Additionally, the size of NBs enables their internalization into cells, allowing them to serve as effective labels for tracking. Several studies have demonstrated the effectiveness of nanosized contrast agents in labeling and tracking various cell types, including stem cells and NK cells.[18,20,24–26] Building on this foundation, we aim to track CAR-T cells using US imaging enhanced by NBs, which could enable timely and cost-effective monitoring of these therapeutic cells.

Prior studies have demonstrated the ability of NBs to be trafficked inside cells *via* phagocytosis or receptor-mediated endocytosis.[26,27] We hypothesize that CAR-T cells may also utilize endocytosis to uptake NBs during co-incubation, enabling non-invasive, real-time monitoring of infused cells. To evaluate this technique, we labeled CD19-targeted CAR-T cells because of their widespread clinical use for Lymphoma and the potential of this monitoring method to enhance an approved immunotherapy (Fig. 1). We then assessed the trafficking of labeled CD19 CAR-T cells using NLC imaging in both a healthy murine model and a Burkitt's lymphoma (RAJI cells) murine model. In healthy tissue, CD19 CAR-T cells exhibited rapid influx post-injection, whereas in tumor tissues, accumulation was slower, highlighting tissue heterogeneity and differences in CD19 CAR-T cell dynamics across tissues. Our findings show that CD19 CAR-T cells remain localized within tumor regions for the full 75 minutes post-infusion, supported by NLC signal from US, as well as flow cytometry and histology. While therapeutic effects are typically observed at later time points, our findings show that

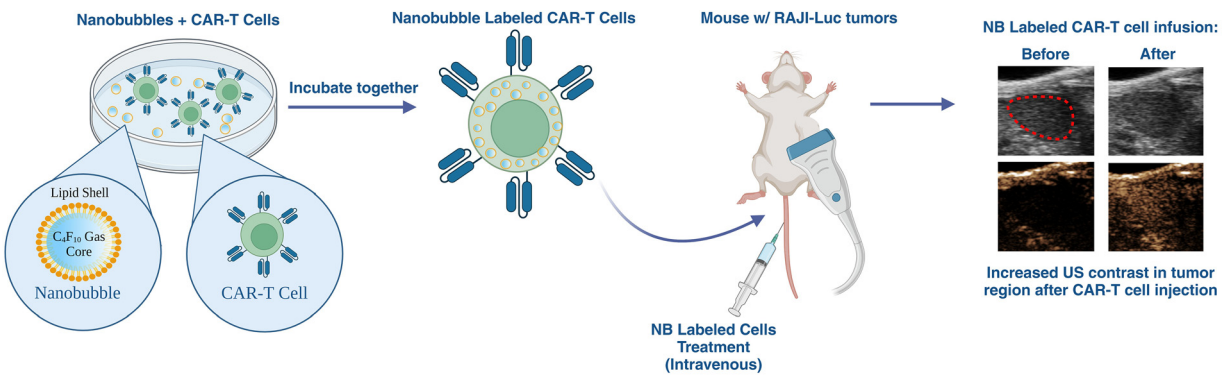

Fig. 1 Schematic illustration of the NB labeling process of CAR-T cells and their injection into tumor bearing mice. Images are not to scale.

CAR-T cells trafficked into and persisted within tumor-associated vasculature and tissue, as indicated by the sustained NLC signal over time. These results demonstrate the feasibility of using this imaging technique for non-invasive, real-time tracking of CAR-T cells, underscoring its potential for clinical application in CAR-T cell therapy monitoring.

Materials and methods

Preparation of CAR-T cells

Peripheral blood mononuclear cells (PBMCs) were isolated from healthy donor whole blood samples mononuclear peripheral blood samples were processed within 24 hours of receipt. The study was approved by the University Hospital Cleveland Medical Center institutional review board and all donors gave written informed consent. T cells were stimulated using Miltenyi TransAct reagent (Miltenyi Biotec; Bergisch Gladbach, Germany). In addition, T cells were supplemented with cytokines (IL2 every other day to a final concentration of 30 IU per μL). The activated T cells were cultured in complete RPMI medium supplemented with 10% fetal bovine serum (FBS; Cytiva; Marlborough, MA) and 1% Penicillin–streptomycin antibiotics (Pen Strep; Cytiva; Marlborough, MA).[28] During labeling, however, the cells were cultured in 3% human serum albumin. Following activation, T cells were cultured with periodic media changes, maintaining a concentration of 1 million cells per mL.

For genetic modification, CD19 CAR Lentiviral particles were produced by transfecting HEK293T cells using Lipofectamine™ 3000 (Thermo Fisher Scientific; Waltham, MA) with a second generation 41BB/CD3zeta containing CAR plasmid and helper plasmids, encoding as VSV-G, GAG/POL, and REV (Addgene; Watertown, MA). The T cells were transduced with the corresponding CD19 lentiviral vector, 1 day after activation, and expanded for a maximum of 10 days before cryo-freezing the cells in liquid nitrogen.[29]

At day 5 and onwards, the expanded CAR-T cells were assessed for viability, CAR-expression, and cytotoxicity. The viability was assessed by trypan blue counts, and the CAR expression was assessed by flow cytometry using anti-FMC63 FITC (Acrobiosystems; Newark, DE) on the Attune Flow Cytometer (Thermo Fisher Scientific). In addition, the functionality of the CAR-T cells was validated for cytotoxicity *via in vivo* survival study.

Preparation of nanobubbles

NBs were prepared according to a previously published protocol.[30] However, we used C_4F_{10} as an alternative gas, which has shown to improve stability compared to C_3F_8.[31,32] Briefly, the lipids DPPA (1,2-dipalmitoyl-*sn*-glycero-3-phosphate; Avanti Polar Lipids Inc.; Pelham, AL), DPPE (1,2-dipalmitoyl-*sn*-glycero-3-phospho-ethanolamine; Avanti Polar Lipids Inc.; Pelham, AL), DSPE-mPEG-2k (1,2-distearoyl-snglycero-3-phosphoethanolamine-*N*-[methoxy(polyethylene glycol)-2000]; Laysan Lipids; Arab, AL), and DBPC (1,2-dibehenoyl-snglycero-3-phosphocholine; Avanti Polar Lipids Inc.; Pelham, AL) were dissolved in propylene glycol (PG; Sigma Aldrich; Saint Louis, MO) at 80 °C in a hot water bath. Simultaneously, a solution of phosphate-buffered saline (PBS; Gibco Life Technologies; Grand Island, NY) and glycerol (Sigma Aldrich; Saint Louis, MO) was heated to 80 °C. Once the lipids were fully dissolved, the PBS-glycerol solution was added to the lipid mixture. The final solution was added to a 3 mL headspace vial and sealed. The gas was then exchanged with C_4F_{10} (Perfluorobutane; FluoroMed; Round Rock, TX) and the vials were activated using mechanical agitation (Vialmix). NBs were isolated by centrifugation 5 minutes at 50 g, unless otherwise noted, and extracted prior to use. Rhodamine-NBs were formulated by incorporating DSPE-PEG-Rhodamine (1,2-dioleoyl-*sn-glycero*-3-phosphoethanolamine-*N*-(lissamine rhodamine B sulfonyl); Avanti Polar Lipids Inc.; Pelham, AL) into the lipid mixture prior to lipid dissolution. The NBs were characterized using dynamic light scattering (DLS; Litesizer DLS 500, Anton Paar) demonstrating plain NBs with no fluorescent label have an intensity-weighted diameter of 293.52 ± 50 nm, while rhodamine-labeled NBs have an intensity-weighted diameter of 258.52 ± 42 nm (Fig. S1). The polydispersity index (PDI) for plain and rhodamine-labeled NBs was 0.16 ± 0.07 and 0.18 ± 0.04, respectively. The zeta potential measured in diethyl pyrocarbonate (DEPC) water was −52.49 ± 0.98 mV for plain NBs and −49.33 ± 0.23 mV for rhodamine-labeled NBs. Based on previously characterized NB formulations using resonant mass measurement (RMM; Archimedes®, Malvern Panalytical), the NBs have a concentration of approximately 3.5×10^{11} NBs per mL.[25,30,33] Additionally, brightfield microscopy (Keyence BZ-X800 Microscope) was used to image the NBs diluted to approximately 3.5×10^9 NBs per mL (Fig. S2).

Labeling CAR-T cells with nanobubbles

CD19 CAR-T cells were thawed in complete RPMI media containing 10% FBS and 1% Pen Strep. After thawing, the cells were left in the complete media for 30 minutes before being centrifuged for 5 minutes at 500 g and collected. The cells were then diluted to 5×10^6 cells per mL in RPMI media with 3% human serum albumin (HSA; Innovative Research; Novi, MI). NBs were added to the cell solution to achieve concentrations of 10k, 15k, or 20k NBs per cell. The NB-cell solution was incubated at 37 °C with 3% CO_2 for 1 hour, with gentle shaking every 15 minutes. After the incubation period, the cells were centrifuged at 230 g for 10 minutes and washed in incomplete media.

In vitro ultrasound imaging setup

The *in vitro* US imaging was conducted in a three well agarose phantom shown in Fig. 2a. The phantom was prepared by dissolving low-temperature gelling agarose (Sigma Aldrich; Saint Louis, MO) at a 2.4% w/v concentration in deionized (DI) water. The agarose solution was then poured into a mold with the desired specifications (Fig. 2a). During imaging, the MS250 US transducer (Vevo® 2100, FUJIFILM VisualSonics) was positioned perpendicular to the wells against the phantom and coupled with US gel. Approximately 50 μL of the cell suspension was placed in the well and imaged using nonlinear contrast (NLC) mode with the following parameters: 4% power, 18 MHz, 1 fps, 35 dB contrast gain, 18 dB 2D gain. The nonlinear

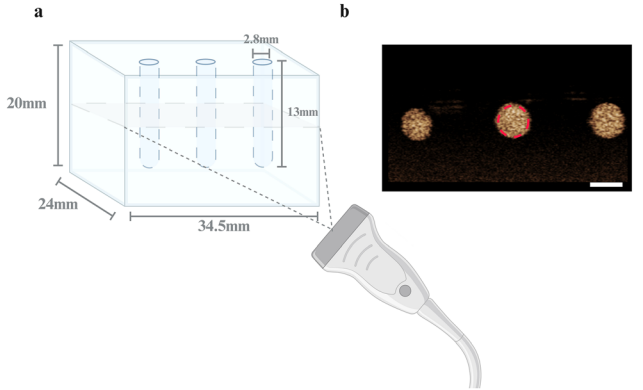

Fig. 2 (a) *In vitro* imaging setup using the 3-well agarose phantom with the transducer placed horizontally at the side of the phantom. (b) NLC cross-sectional image produced by the *in vitro* imaging setup using the phantom with all 3 wells filled with NB contrast agent. The red circle over the center well indicates the ROI used to analyze the average signal intensity (scale bar = 2.8 mm).

contrast mode on the Vevo 2100 uses a form of amplitude modulation to generate the images.[34]

In vitro ultrasound imaging

NB-labeled CAR-T cells were evaluated *in vitro* utilizing two distinct methods within the US imaging setup: (a) imaging the labeled cells at discrete time-points over 24 hours, and (b) minimum detectable concentration. In the discrete time-point study, cells were labeled with 10k, 15k, and 20k NBs per cell. After labeling, the cells were diluted to 1×10^6 cells per mL in complete RPMI media and transferred to a 96-well plate with 200 μL per well. The samples were imaged immediately after labeling, and then at 0.5, 1, 2, 3, 6, and 24 hours post-labeling. Between imaging sessions, the cells were kept in an incubator at 37 °C with 5% CO_2. To evaluate the minimum detectable concentration the cells were labeled with 20k NBs per cell. After labeling, the cells are diluted to 1×10^6, 10^5, 10^4, and 10^3 cells per mL in PBS and evaluated in the phantom. For each study the control samples containing only CAR-T cells underwent the same labeling conditions and imaging parameters, but without the addition of NBs.

Nanobubble stability in physiological conditions

NBs were resuspended in Plasmalyte (Baxter Healthcare; Deerfield, IL) at a concentration of 1×10^{11} NBs per mL and incubated at 37 °C with 5% CO_2. Stability was assessed at 0, 1, 2, 3, and 6 hours using US imaging and DLS. The NBs were diluted to 1×10^8 NBs per mL in PBS for US imaging and to 1×10^7 NBs per mL for DLS analysis (Fig. S3). These dilutions were applied consistently across all time points.

In vivo ultrasound imaging

Male and female NCG mice (strain code: 572; Charles River) were handled in according to a protocol approved by the Institutional Animal Care and Use Committee (IACUC) at Case Western Reserve University. The RAJI cells (ATCC) were injected intravenously (2×10^6 cells in 150 μL of PBS) to establish disease over the course of three weeks. Tumor growth was monitored using bioluminescence imaging (PerkinElmer), US imaging was performed around the left kidney after confirmation of tumor growth in this region by bioluminescence imaging. Approximately 0.7–1 $\times$ 10^7 NB labeled CAR-T cells were injected intravenously, and mice were imaged during and after labeled cell infusion at the following time points: 0, 5, 15, 30, 45, 60, and 75 minutes. Each time point had $n = 4$, except for the 5-minute time point, where $n = 3$. Liver imaging studies were conducted separately in non-tumor bearing NCG mice. The liver was imaged at the same time points as the tumor-bearing mice ($n = 3$).

US imaging was conducted using the Vevo 2100 ultrasound system with the MS250 transducer in NLC mode. The same parameters were used as the *in vitro* studies: 4% power, 18 MHz, 1 fps, 35 dB contrast gain, and 18 dB 2D gain. All animals underwent hair removal in the region of interest (ROI) and were anesthetized *via* inhalation of 2% isoflurane mixed with 1.5 L min^{-1} of air and were placed on a heating platform to maintain a stable temperature throughout the imaging timeframe.

Image analysis

NLC images were quantified using FUJIFILM VisualSonics Vevo LAB software. For *in vitro* data analysis, an ROI was drawn, as shown in Fig. 2b, with an additional ROI selected outside the well of the phantom to quantify the background signal. The background was subtracted from the average signal intensity within the well to provide comparability between samples. For the analysis of *in vivo* studies, ROIs were manually drawn over each area of interest (liver, kidney, and tumor) to exclude surrounding tissues. The baseline NLC signal in each tissue was acquired and quantified prior to the infusion of labeled cells. Following this background acquisition, the nonlinear signal intensity was measured for the infusion of labeled cells, with the maximum value used for the 0 min discrete time point. The mean nonlinear signal was then calculated for frames captured at 5, 15, 30, 45, 60, and 75 minutes post-infusion. The baseline signal was used to compute the signal-to-baseline ratio over the 75-minute period and to adjust the NLC signal over time by subtracting the background.

Confirmation of CAR-T cell labeling

Labeling efficiency of CAR-T cells with Rhodamine-conjugated NBs was assessed through flow cytometry and microscopy for flow cytometry analysis, following the labeling procedure described in the methods. A minimum of 200 000 events per sample were collected to ensure robust data. Flow cytometry data were analyzed using Attune software and formalized with FlowJo software (BD Biosciences, NJ). Rhodamine-conjugated NB-labeled CD19 CAR-T cells were compared to unlabeled CD19 CAR-T cells, which served as controls to verify the labeling process. Uptake of Rhodamine-conjugated NBs by CAR-T cells was quantified through the positive shift in Rhodamine fluorescence, with distinct separation from the control group, confirming successful and efficient labeling.

CAR-T cell labeling was also confirmed by confocal microscopy. Here, CAR-T cells were labeled with rhodamine-labeled NBs and then diluted to 1×10^6–2×10^6 cells per mL in PBS. The cells were fixed onto a glass slide using 4% paraformaldehyde (PFA; Fisher Chemicals, Pittsburgh, PA) for 30 minutes, washed with PBS three times, stained using DAPI mounting media (Fisher Chemical; Pittsburgh, PA) and sealed with a glass coverslip. Slides were kept at 4 °C until imaging. Imaging was performed on a Leica SP8 confocal microscope.

Assessment of macropinocytosis-mediated nanobubble uptake in CAR-T cells

Macropinocytosis, an endocytosis pathway, was evaluated as a potential mechanism of NB uptake, as it is known to be upregulated in activated T cells and enables internalization of particles between 200 nm–20 μm.[35,36] To assess this pathway, CAR-T cells were pre-incubated with or without 50 μM EIPA (5-(*N*-ethyl-*N*-isopropyl)amiloride; Sigma Aldrich; Saint Louis, MO), a macropinocytosis inhibitor, in incomplete RPMI medium for 15 minutes. Cells were then labeled with C_4F_{10} rhodamine NBs at a ratio of 20k NBs per cell for 1 h. Labeled cells were subsequently analyzed by US imaging, flow cytometry, and confocal microscopy as previously described.

Biodistribution of CAR-T cells *in vivo*

Prior to injection, NBs were isolated by centrifugation for 10 minutes at 50 g and used to label CAR-T cells following the same labeling protocol described above. Male NCG mice (6–8 months old) were intravenously injected with approximately 1×10^7 NB-labeled CAR-T cells. For biodistribution in healthy mice ($n = 3$), NLC imaging was performed over the liver during and after infusion at 0, 5, 15, 30, 45, 60, and 75 minutes. The percent change in NLC signal for healthy mice imaged over the liver is shown in Fig. S4. For tumor-bearing mice, additional NCG mice ($n = 3$) were intravenously inoculated with 2×10^6 RAJI cells (ATCC) in 150 μL PBS and monitored for 3 weeks until disseminated disease was established. Tumor localization adjacent to the kidney was confirmed by bioluminescence (Spectrum) imaging prior to US.

At 75 minutes post-infusion, ~0.5 mL of blood was collected *via* cardiac puncture. Bone marrow was flushed from femurs with 1 mL PBS, and organs including lungs, kidneys, liver, and spleen were harvested. In tumor-bearing mice, the RAJI tumor mass adjacent to the kidney was also excised. Each organ was weighed and divided, with portions allocated for histology (fixed in 10% neutral buffered formalin) and for flow cytometry (processed fresh).

For flow cytometry, tissues were mechanically dissociated to generate single-cell suspensions. Following digestion, suspensions were filtered through a 70 μm strainer and treated with RBC lysis buffer (ChemCruz; Dallas, TX, at 5 min, RT). The cells were then washed with FACS buffer (PBS + 2% FBS). Cell suspensions were incubated with DNase I (100 U mL^{-1}, Worthington Biochemical; Lakewood, NJ) and collagenase type IV (1 mg mL^{-1}, 30 min, 37 °C, Worthington Biochemical) to reduce clumping and improve cell recovery. These suspensions were spun down and stained with BV421-conjugated anti-human CD45 (BioLegend; San Diego, CA; clone HI30, 1 : 100; 15 min; RT). After washing, samples were analyzed on an Attune NxT flow cytometer (Thermo Fisher Scientific), acquiring at least 100 000 events per sample. For quantitative comparison, a consistent sample volume was analyzed (*e.g.*, 100 μL of blood or a defined fraction of each organ digest), and absolute CAR-T cell counts were extrapolated to yield normalized values expressed as cells per mL of blood or cells per g of tissue. Data was processed using FlowJo v10, with background fluorescence determined using uninfused controls and *in vitro* control gates. Samples that failed quality control criteria, such as incomplete tissue dissociation or poor viability, were excluded.

Histology and immunohistochemistry

Immunohistochemistry (IHC) was performed by HistoWiz, Inc. using a Leica Bond RX automated stainer (Leica Microsystems) with standard protocols. Paraffin-embedded tissue sections (4 μm) underwent heat-induced epitope retrieval (HIER) in EDTA-based buffer (pH 9, Leica AR9640) at 100 °C for 20 minutes (CD19) or 30 minutes (CD3). Endogenous peroxidase activity was blocked with peroxide buffer (Leica Microsystems). CD19 staining was performed with a ready-to-use antibody (Agilent, GA65661-2), and CD3 with a 1 : 50 dilution (Leica, NCL-L-CD3-565), each followed by DAB polymer detection, hematoxylin counterstaining, and coverslipping (Sakura Tissue-Tek Film). Slides were scanned at 40× magnification on an Aperio AT2 scanner (Leica Microsystems).

Cell densities were quantified in QuPath, where representative tumor and organ regions were annotated and DAB-positive cells automatically detected.[37] The cell counts were exported for comparison with imaging data.

For US analysis, matched frames were selected at baseline (0 min) and post-infusion (75 min). ROIs were defined, and total NLC signal was quantified in MATLAB. Background-corrected NLC values were correlated with IHC-derived cell counts using Pearson's correlation in GraphPad Prism.

In vitro assessment of viability and differentiation *via* flow cytometry

To assess CAR-T cell proliferation, both NB-labeled CAR-T cells and unlabeled control T cells were cultured and counted every two days following culture initiation. Cell counts were performed using the Countess (Invitrogen; Waltham, MA) with trypan blue exclusion to distinguish viable cells from non-viable ones.

To evaluate differentiation and viability following labeling, CAR-T cells were stained with the following reagents: CD3 (APC), CD4 (APCeflour780), CD8 (BV510), CD45RA (BV605), CCR7 (PE), CAR antigen (FITC), and CD27 (AF700) antibodies, as well as the viability dye (7-AAD), (BD BioSciences; Franklin Lakes, NJ). Flow cytometry data were analyzed using FlowJo software (BD Biosciences; Franklin Lakes, NJ). The memory panel, assessing differentiation markers, was performed 4 days after labeling to monitor any potential effects over time. Additionally, the study was verified across a range of NB

concentrations (1k, 5k, 10k, and 20k NBs per cell) to determine if the labeling process had any concentration-dependent impact on CAR-T cell differentiation. For this study, CAR-T cells were labeled using C_3F_8 NBs. The labeling protocol consisted of a 1-hour incubation on a shaker set to 225 rpm (linear rocking). The cells were incubated in complete RPMI medium, with a seeding density of 5×10^6 cells per mL, with the incubator maintained at 5% CO_2.

In vivo efficacy and biodistribution

An efficacy study was conducted to verify the *in vivo* functionality of the NB-labeled CAR-T cells compared to the unlabeled CAR-T cell control group. Male and female mice received intravenous injections *via* the tail vein with 1 million luciferase-expressing RAJI tumor cells. In the inoculated mice used for the US imaging, CAR-T cells are injected 1 week following tumor inoculation. Approximately 10 million CAR-T cells, labeled with 20k NBs per cell following the same protocol used in the differentiation study, were administered intravenously *via* the tail vein. Progression of the tumor burden was monitored weekly by weight measurements and bioluminescence imaging using the IVIS Spectrum Imager (PerkinElmer; Waltham, MA). Mice were injected with 10 mg kg^{-1} of D-Luciferin (Invitrogen; Waltham, MA) subcutaneously. After 10 minutes, the images were taken and then analyzed with Living Image (PerkinElmer). Background values were taken prior to luciferase imaging to remove noise from the bioluminescent regions of interest. Tumor burden was quantified in terms of luciferase intensity (radiance).

Statistical analysis

NLC data was plotted and analyzed using Excel and GraphPad Prism, with each experiment conducted three times unless otherwise specified. Unpaired two-tailed *t*-tests were utilized to compare the two groups. Data is presented as mean ± SEM (standard error of the mean), unless stated otherwise, and a *p*-value of less than 0.05 was deemed statistically significant. Outliers were assessed and removed using Grubbs' test with a significance threshold of $p = 0.05$. To minimize bias and ensure analytical rigor, image analysis and ROI selection were performed using predefined criteria prior to correlation with histological outcomes.

Results and discussion

In vitro evaluation of labeled CAR-T cells

The labeling efficiency of CAR-T cells with NBs was first evaluated *in vitro* using an agarose phantom (Fig. 3a and b). Unlabeled control CAR-T cells showed negligible signal, with NLC values of 10^6 cells per mL (19.05 ± 6.17 a.u.) and 10^3 cells per mL (33.64 ± 2.40 a.u.). In comparison, NB-labeled CAR-T cells demonstrated significantly higher signals at 10^6 cells per mL (64 032.52 ± 20 859.39 a.u.) and 10^3 cells per mL (105.09 ± 60.02 a.u.), showing a 3362-fold and 3-fold increase, respectively, over unlabeled cells.

Based on these results, the *in vitro* detection threshold is 10^3 cells per mL, determined from the labeled-to-unlabeled NLC signal ratio. Despite only ~6 cells per imaging slice, labeled cells produced a signal ~2.3× higher than unlabeled cells, even though some cells may move out of the imaging plane, highlighting the sensitivity of this approach. This demonstrates

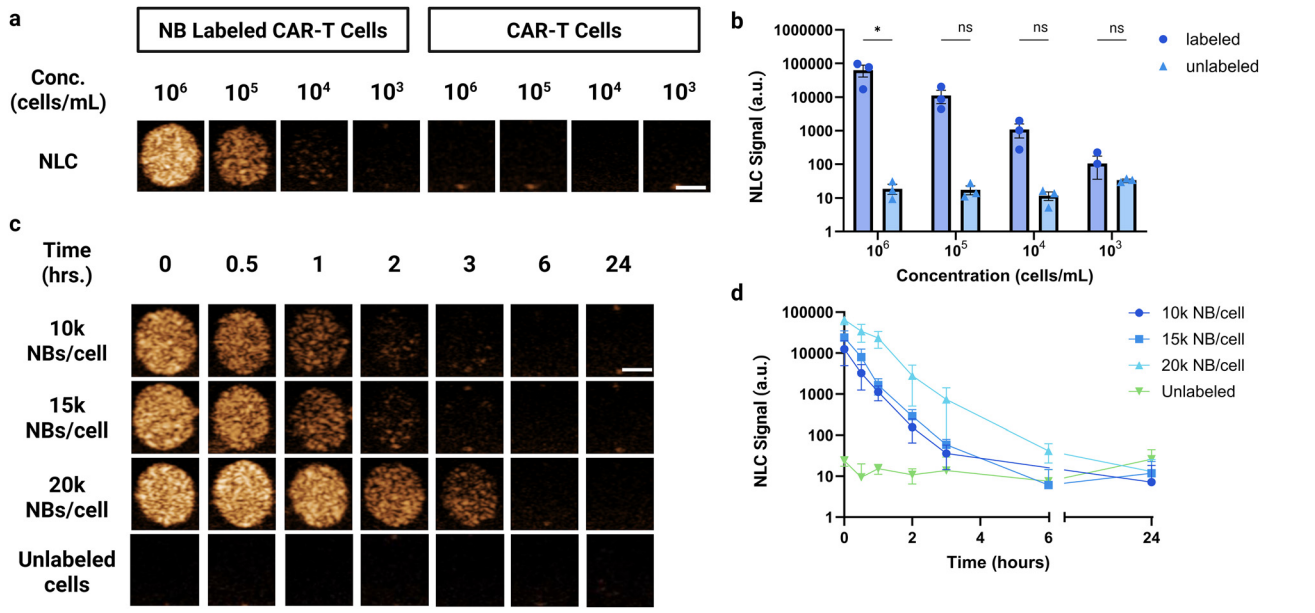

Fig. 3 (a) NLC images of CAR-T cells labeled with 20k NBs per cells and unlabeled CAR-T cells at concentrations of 1×10^3–1×10^6 cells per mL (scale bar = 1.4 mm). (b) Average NLC signal (a.u.) in each well at different concentrations of labeled and unlabeled cells, normalized by subtracting the background signal from the phantom ($n = 3$). (c) CAR-T cells labeled with various concentrations of NB per cell during the co-incubation process. (scale bar = 1.4 mm). (d) Average NLC signal (a.u.) over time for CAR-T cells labeled with 10k, 15k, and 20k NBs per cell and unlabeled cells, with background subtraction performed as in (b) ($n = 3$). All NLC signal and values shown here reflect imaging under the specific ultrasound parameters used in this study; alternative imaging parameters may alter signal dynamics.

a high detection sensitivity compared to other techniques, which report thresholds between 10^4 and 10^5 cells per mL.[9,12]

To evaluate the stability of the signal within labeled cells and the effects of NB concentration on the labeling process, CAR-T cells were incubated at 37 °C with 10k, 15k, and 20k NBs per cell and imaged at 0.5, 1, 2, 3, 6, and 24 hours (Fig. 3c). All samples exhibited high NLC signal immediately after labeling. The signal gradually decreased to baseline over 24 hours (Fig. 3d). Cells labeled with 20k NBs per cell showed the highest average NLC signal at all time points. At 6 hours, the signal in these cells remained 5.5 times that of the unlabeled cells. The average signal for the 10k and 15k NB per cell samples decayed faster and returned to baseline at 6 hours. From this study we opted to use the 20k NBs per cell concentration for labeling CAR-T cells.

In vivo detection of labeled CAR-T cells in non-tumor bearing mice

Using the optimized concentration of 20k NBs per cell for labeling CAR-T cells, the CAR-T cells were evaluated *in vivo* through intravenous administration to immunodeficient mice (Fig. 4a). The liver was selected for initial evaluation due to its low baseline NLC signal with US. After infusion, the liver NLC signal increased by an average of 13-fold over baseline, followed by a gradual decrease over 75 minutes (Fig. 4b). This study serves as a proof-of-concept to demonstrate the feasibility of tracking CAR-T cells *in vivo* using US. It is likely that the signal detected during this time course represents CAR-T cells transiently passing through the liver as current research suggests that CAR-T cells begin to accumulate to higher levels in the liver approximately 3–24 hours post-infusion.[8,35] In our studies, the liver signal drops to baseline at approximately 30–45 minutes following injection, indicating that majority of the cells have moved out of the general circulation and into other tissues around this time. Flow cytometry biodistribution analysis performed after 75 minutes (Fig. 4c) confirmed low CAR-T cell concentrations in the liver (~544 cells per g) and blood (~46 cells per mL). Importantly, the blood concentration was below the *in vitro* limit of US detection (10^3 cells per mL), consistent with the absence of detectable signal at this later time point. At early time points, the low levels in the liver and blood are consistent with *ex vivo* qPCR studies in healthy male mice infused with the same number of CAR-T cells.[35] Our approach allows us to visualize early time points post-infusion, providing crucial insights into initial CAR-T cell interactions with tissues. While CAR-T cell efficacy is often assessed at later time points, understanding these early dynamics remains essential for optimizing treatment outcomes, ensuring effective targeting from the outset, and addressing potential challenges such as poor infiltration or early off-target effects. Currently, CAR-T cells are known to accumulate in tissues such as the lung within the first day of therapy, however earlier time points have not been rigorously studied.[7,8,35,36] Future studies will extend these time points to provide a more comprehensive understanding of CAR-T cell dynamics over longer durations.

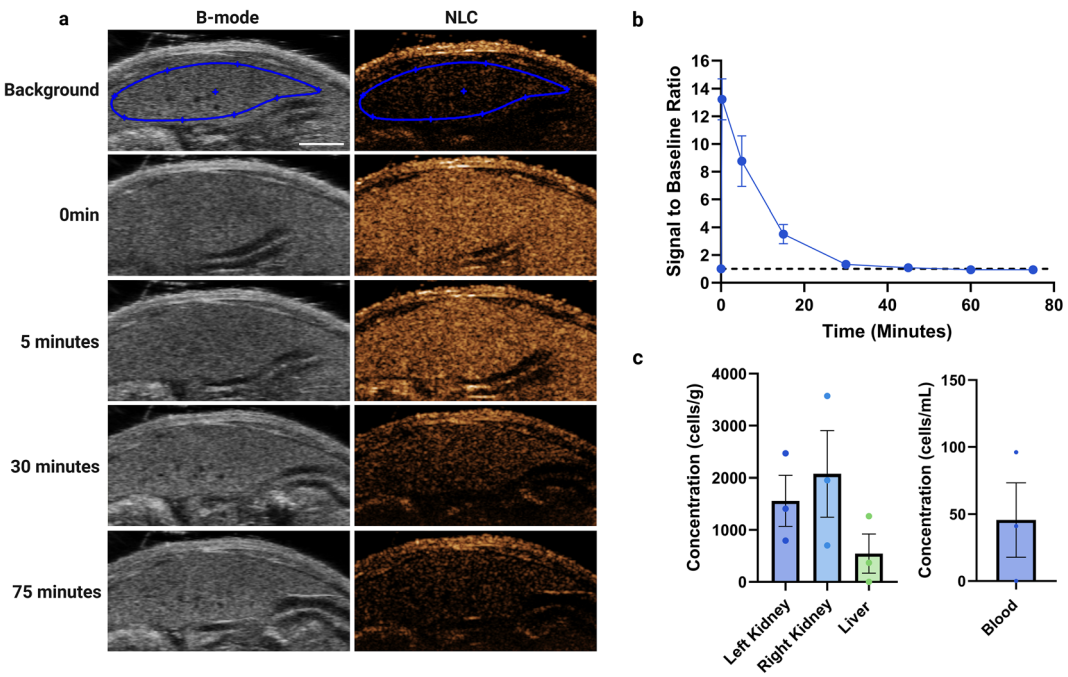

Fig. 4 (a) B-mode and NLC images of the liver of an NCG mouse over 75 minutes before and after the infusion of labeled CAR-T cells (scale bar = 3.5 mm). (b) Average signal intensity of the liver over time following infusion of labeled CAR-T cells (n = 3), analyzed using the ROI depicted in the background image of Fig. 4a. Signals at all time points were normalized by dividing by the baseline signal. (c) CAR-T cell biodistribution in the kidneys, liver, and blood of healthy mice was assessed by flow cytometry after infusion and 75 minutes of US imaging (n = 3). Kidney and liver values are reported as cells per g of tissue (normalized to tissue weight), and blood values as cells per mL (normalized to sample volume).

In vivo detection of labeled CAR-T cells in tumor mouse models

To demonstrate initial proof of concept in a tumor model, NB-labeled CAR-T cells were evaluated in an immunodeficient mouse model using systemic RAJI lymphoma tumors and CD19 CAR-T cells. This model system is beneficial as CD19 CAR-T cells are known to be efficacious against these tumor cells and the CD19 CAR-T cells can traffic to the tumors.[38,39] In mice, systemic administration of RAJI cells resulted in tumor formation in various organs, but tumors consistently formed in and adjacent to the kidneys. We focused our imaging on this region, with baseline tumor distribution visualized *via* IVIS imaging (Fig. S5a). US imaging was carried out during infusion and at 5, 15, 30, 45, 60, and 75 minutes post-infusion. Following imaging, the presence and distribution of both CD19+ tumor cells (Fig. S5b and c) and CD3+ CAR-T cells were confirmed by flow cytometry and histology.

Fig. 5 shows representative B-mode and NLC images and analysis for a single mouse. Both tumors adjacent to the kidney and the kidney itself were imaged at each time point. All regions exhibited elevated NLC signal during infusion (Fig. 5b). The variability in image contrast among these regions highlights tissue heterogeneity, which can influence the rate of CAR-T cell infiltration into tumors. This variability is evident in the tumor infusion plot, where regions show different increases in NLC signal. These findings align with published studies highlighting the heterogeneous nature of RAJI tumors.[40–42] During the initial 30 second infusion, the kidney exhibited a 3-fold increase in NLC signal suggesting we are detecting the CAR-T cells in circulating transiting through the kidney. Conversely, tumors located near the kidney cortex or adjacent to the kidney itself (denoted as 'tumor 1') show reduced NLC signal likely due to differences in vascular density.

Following the infusion, images were acquired intermittently over 75 minutes. After 5 min, the signal intensity increased to 5-fold higher levels compared to baseline (Fig. 5c). This latent, but substantial increase in signal suggests a slower but notable cell penetration into the tumor. NLC images (Fig. 5a) further illustrate the extensive infiltration into the large adjacent tumor at the 5 minute mark. Over time, a spike in NLC signal is observed across all tumors. As the cells become more homogeneously distributed in the blood following the infusion, the signal decreases but stabilizes without dropping below the baseline, indicating persistent but slow CAR-T cell infiltration. Interestingly, 'tumor 2' in the kidney shown in Fig. 5, shows an increase in signal intensity starting at the 45-minute mark, potentially signaling the onset of cell migration to this area.

Similarly, after the initial spike from the bolus injection and a temporary decrease as the cells distribute uniformly in the bloodstream (while maintaining a signal twice the baseline), the kidney gradually increases in NLC signal between 15 and 45 minutes. This NLC signal remains stable from 45 to 75 minutes, signifying ongoing CAR-T cell filtration through the kidney and indicating their persistent presence and potential interaction within the kidney microenvironment.

The mean NLC signal for labeled CAR-T cell distribution in RAJI tumors across seven mice is shown in Fig. 6. Consistent

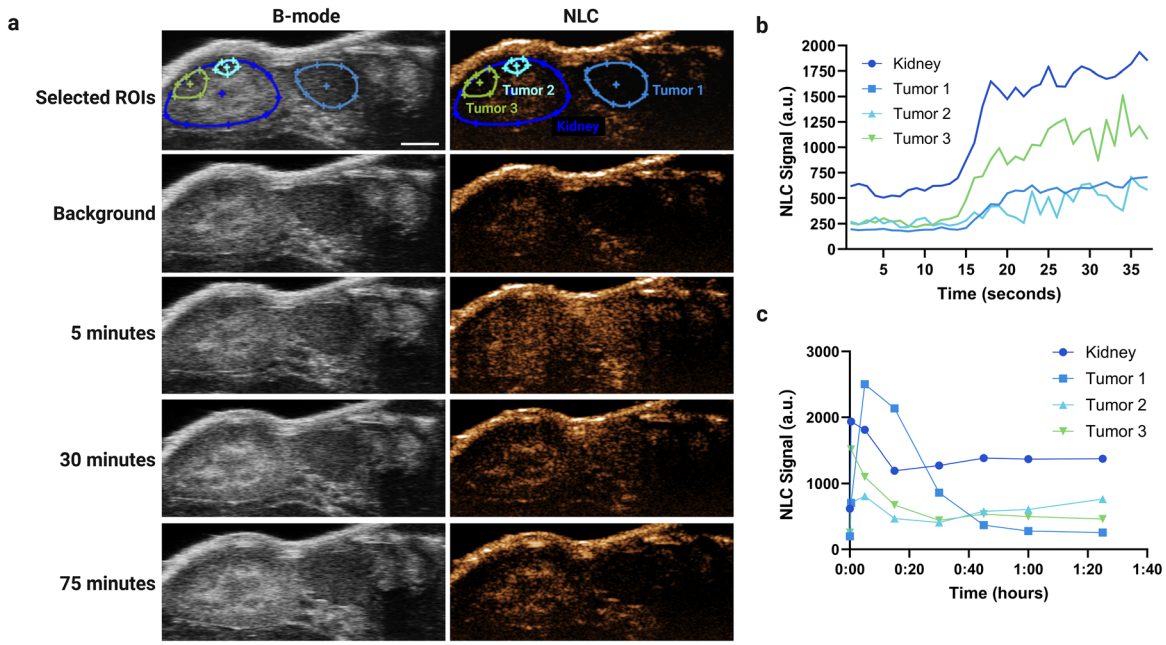

Fig. 5 (a) B-mode (L) and CEUS (R) images of the left kidney and tumors of an NCG mouse over 75 minutes. The ROIs (in blue) shown in the images highlight selected areas for analysis in panels (Fig. 5b) and (Fig. 5c). (scale bar = 2.5mm) (b) Infusion of labeled CAR-T cells into the ROIs depicted in (Fig. 5a) for the kidney and tumors. (c) NLC signal intensity within the ROIs at various time points over 75 minutes, where time point 0 represents pre-infusion, and subsequent points are post-infusion of the labeled CAR-T cells.

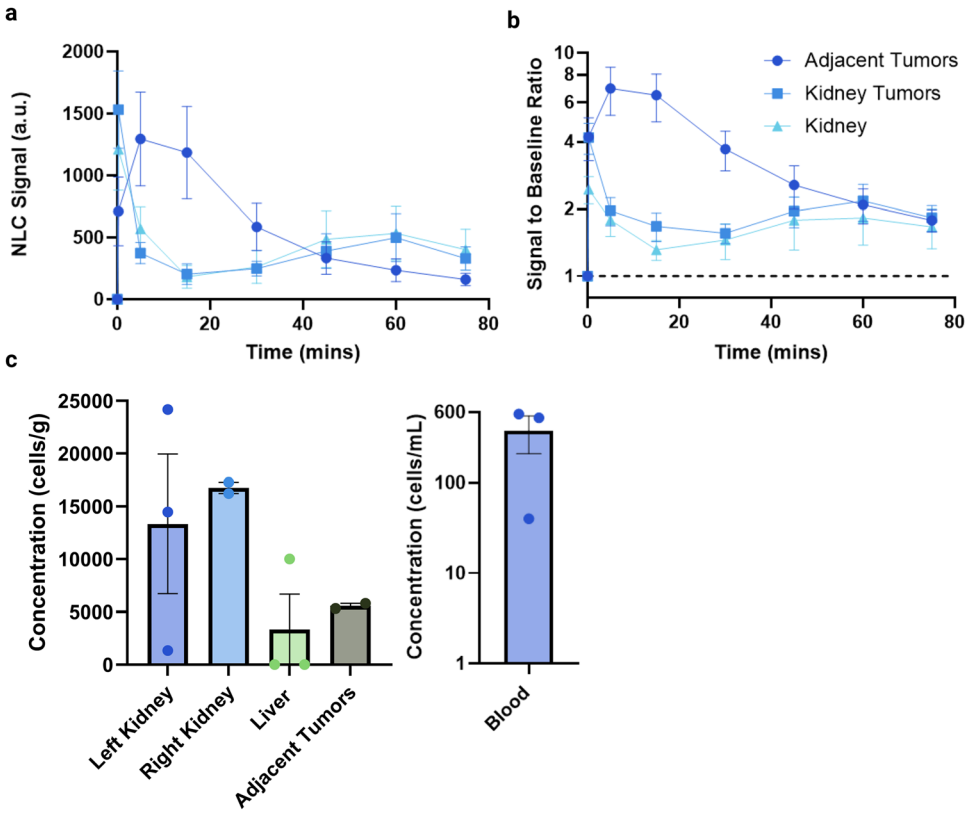

Fig. 6 (a) Average NLC signal (a.u.) in tumor-bearing mice over 75 minutes. For each mouse, the background NLC signal was measured pre-injection and subtracted from the NLC signal at each time point to normalize the data. Variation in sample numbers (mice imaged, n = 7; kidney tumors, n = 12; adjacent tumors, n = 8; kidneys, n = 7) reflects biological variability in metastatic localization and the number of visible tumors per mouse. (b) Average signal-to-baseline ratio for tumor-bearing mice over 75 minutes. Ratios were calculated by dividing the NLC signal (a.u.) at each time point by the pre-injection baseline; values below 1 indicate signal lower than baseline. (c) CAR-T cell distribution in the kidneys, liver, adjacent tumors, and blood was assessed by flow cytometry after infusion and 75 minutes of US imaging. Kidney, liver, and tumor values are reported as cells per g of tissue (normalized to tissue weight), and blood values as cells per mL (normalized to sample volume). Flow cytometry was performed on three mice (n = 3); only two developed adjacent tumors, therefore n = 2 is reported for that group.

with the individual example described above, post-infusion data normalized to background (Fig. 6a) demonstrated that tumor signal peaked within 5 minutes, reflecting the influence of tumor vascular heterogeneity on CAR-T cell distribution. Across tissues, the signal-to-baseline ratios (Fig. 6b) highlighted relative increases above intrinsic NLC signal. Across all mice, a pronounced spike in NLC signal was observed immediately after bolus infusion, which then stabilized but consistently remained above baseline in the tumor region throughout the 75 minute observation period. In contrast, signals in the healthy liver returned to baseline within 30–45 minutes, underscoring that sustained signal in tumor-bearing tissues reflects prolonged persistence of CAR-T cells.

Consistent with *in vivo* NLC imaging, flow cytometry of CD3+ CAR-T cells after imaging (Fig. 6c and Fig. S6b) revealed elevated levels in all tissues of tumor-bearing mice compared to healthy controls, reflecting prolonged persistence of cells in circulation, likely driven by tumor-associated chemokines.[8,35] Low levels of tumor cells were also detected in the blood, which may help sustain CAR-T cells in circulation longer than in healthy mice (Fig. S5b).

In the blood, CAR-T cells were ~8-fold higher than in healthy mice, with tissue fold changes of ~8-fold in the kidneys and ~6-fold in the liver (Fig. S6). At 75 minutes in healthy mice, blood and liver harboured very low CAR-T cell numbers, below those in tumor-bearing mice, corresponding to the rapid decline of liver NLC signal to baseline. Compared to healthy mice, these elevated blood levels in tumor-bearing mice suggest that circulating CAR-T cells contribute to the sustained NLC signal observed in tumor-associated regions.

Histological CAR-T cell distribution and NLC correlation

Representative IHC and H&E images of kidneys, internal tumors, and adjacent tumors are shown in Fig. 7a. DAB staining for CD3 highlights CAR-T cells, with DAB + haematoxylin providing counterstain and H&E showing tissue morphology. The kidney exhibits more prominent DAB signal, likely reflecting its larger vascular supply compared to the smaller, less vascularized internal tumors located in the cortical region. Internal tumors within the kidney display more sporadic CAR-T cell populations, with less consistent staining patterns. Adjacent tumors show more prominent CAR-T cell populations than internal tumors, though these cells visually align with red

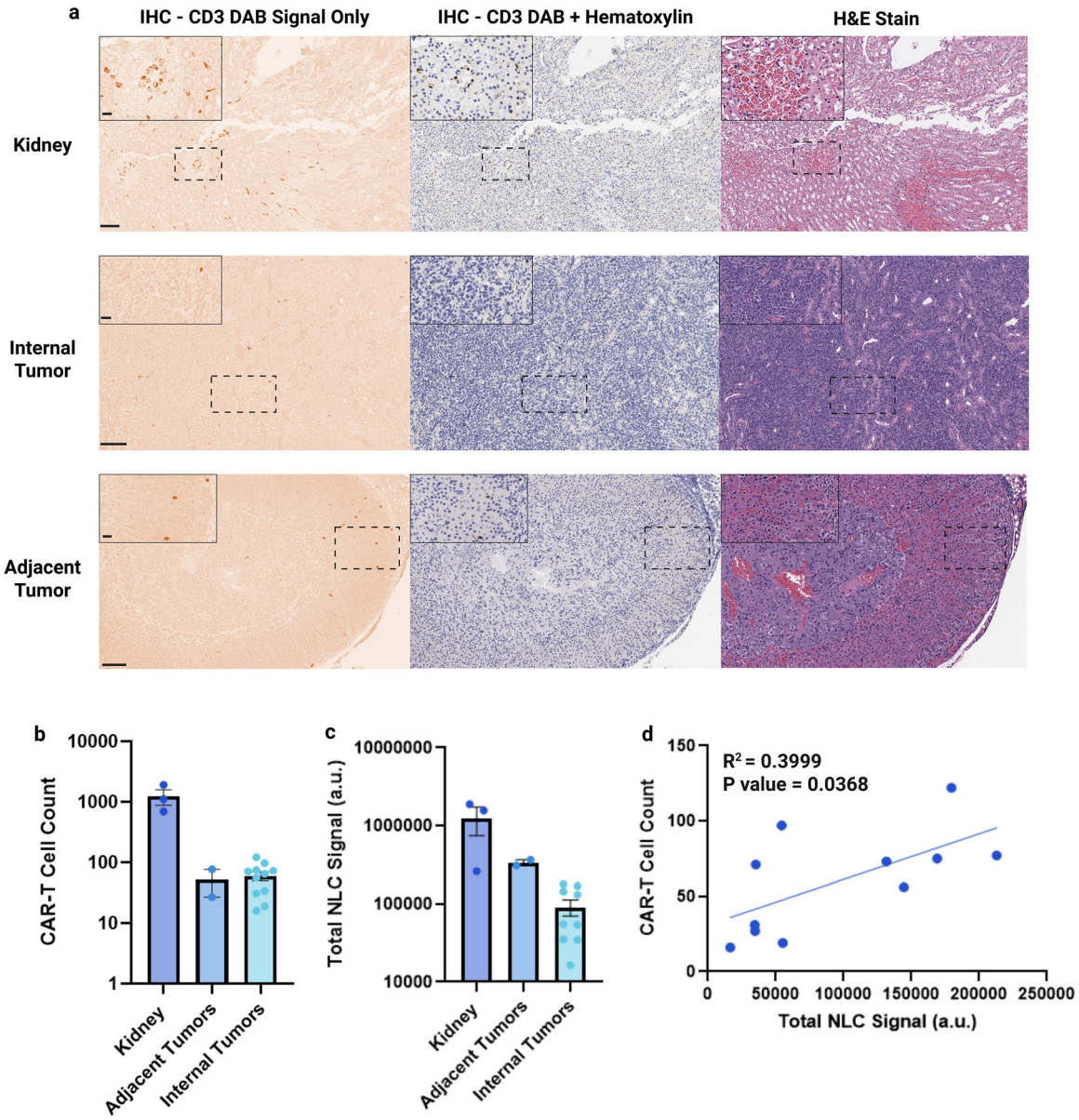

Fig. 7 (a) IHC and H&E images of kidneys, internal tumors, and adjacent tumors. Columns show DAB staining for CAR-T cells, DAB + hematoxylin counterstain, and H&E stain, respectively (Large images: scale bar = 100 μm; zoomed-in images: scale bar = 20 μm.) (b) Quantification of CAR-T cell counts per ROI (kidney tumors, n = 9; adjacent tumors, n = 2, due to limited adjacent tumor availability; kidneys, n = 3). (c) Total NLC signal (a.u.) measured in the same ROIs used for cell counting, normalized by subtracting each ROI's pre-injection NLC value from its 75-minute post-injection value (kidney tumors, n = 9; adjacent tumors, n = 2, due to limited adjacent tumor availability; kidneys, n = 3). (d) Quantification of CAR-T cell counts per ROI compared with total NLC signal from US data, with a correlation analysis (r^2 = 0.3999, p = 0.0368).

blood cell striations observed in H&E sections, suggesting localization within the vasculature.

Quantification of CAR-T cell counts per ROI (Fig. 7b) corresponds with the DAB staining patterns, with kidneys having the highest counts, followed by internal tumors, and adjacent tumors. The total NLC signal per ROI from US (Fig. 7c) similarly shows the highest signal in the kidneys, followed by adjacent and internal tumors, demonstrating that the NLC signal and histological CAR-T cell counts correspond across regions. Correlation analysis (Fig. 7d) demonstrates a significant relationship between histologically measured CAR-T cell numbers and total NLC signal (r^2 = 0.3999, p = 0.0368), indicating that both tissue-localized and circulating CAR-T cells contribute to the NLC signal.

Nanobubble labeled CAR-T cell phenotyping and validation

To confirm that NBs were internalized by CAR-T cells, we used rhodamine-conjugated NBs in addition to detecting nonlinear signal *via* US. Both flow cytometry and confocal microscopy were employed to verify NB labeling (Fig. 8a and b). The presence of intracellular rhodamine signal supports the internalization of the NBs by the CAR-T cells. To investigate the

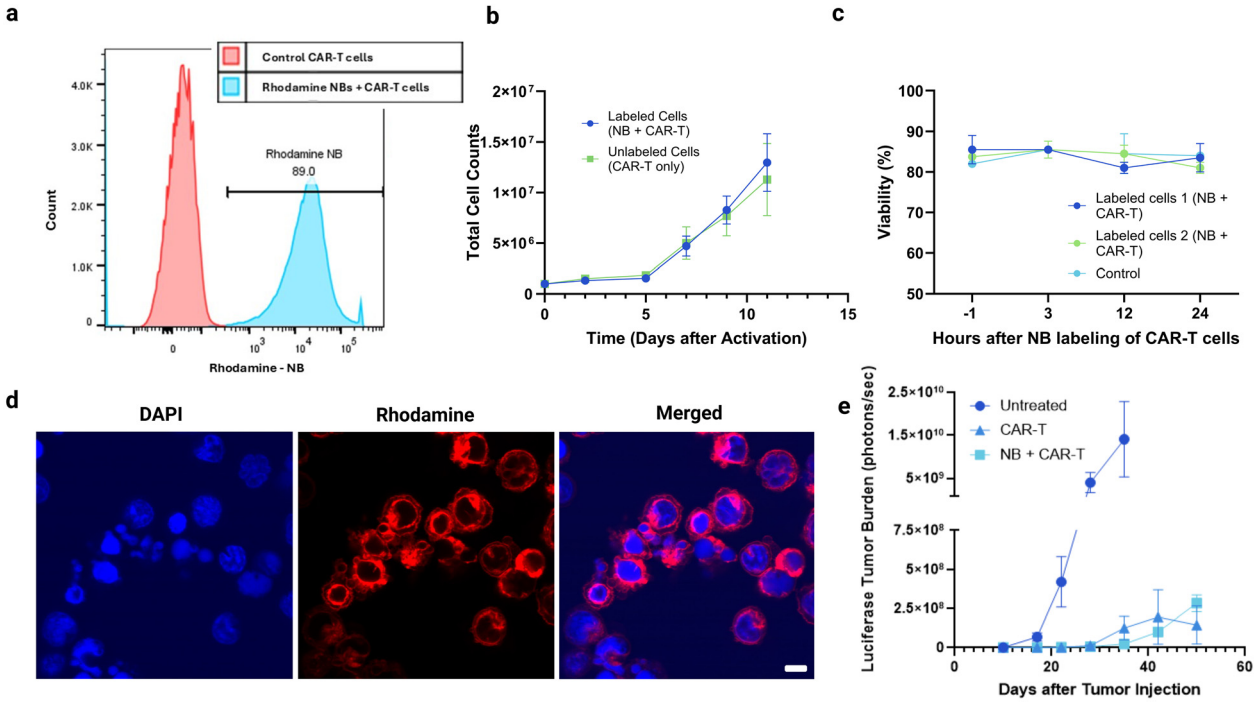

Fig. 8 (a) Flow cytometry panel showing the colocalization of CAR expression and rhodamine NB NLC signal. (b) Proliferation assay comparison of labeled and control CAR-T cells (n = 3). Expansion showed a non- significant effect on the growth of the cells after activation. (c) Viability of labeled cells and unlabeled cells (control) following the labeling procedure (n = 3). NBs did not impact the viability of the cells as measured by trypan blue. (d) Confocal microscopy of rhodamine NB-labeled CAR-T cells: red = rhodamine, blue = DAPI (scale bar = 5 μm) (e) Mice were intravenously injected with RAJI-luciferase to establish tumor burden. Untreated mice (n = 6) and mice treated with control CAR-T (n = 5) or NB CAR-T (n = 5) were monitored for survivability, with both treated groups exhibiting similar survival compared to untreated controls. Tumor burden was assessed using luciferase imaging (photons per s).

uptake mechanism, CAR-T cells were labeled in the presence of EIPA, a macropinocytosis inhibitor (Fig. S7). Cells labeled without EIPA showed a 3-fold higher median fluorescence intensity by flow cytometry and a 2-fold higher NLC by US compared to EIPA-treated cells. Confocal imaging further revealed less rhodamine signal in EIPA-treated cells, supporting macropinocytosis as a substantial contributor to NB internalization.

To confirm that NB internalization did not affect the phenotype or functionality of CAR-T cells, we compared the proliferation, viability, and cytotoxic activity of the NB-labeled CAR-T cells to unlabeled control cells. As expected, the NB-labeled CAR-T cells expanded similarly to the control cells, with both groups exhibiting an approximately 10-fold expansion over 14 days (Fig. 8b; p = 0.4703, t-test, ns). Additionally, to verify that the NB labeling process does not impact cell viability, the cells were stained with trypan blue at 0, 3, 12, and 24 hours after NB labeling. Fig. 8c illustrates that there was no difference in viability between the labeled and unlabeled CAR-T cells (p = 0.77, t-test, ns). This approach allowed for a direct comparison of proliferation rates between labeled and unlabeled CAR-T cells, ensuring that the labeling process did not adversely affect cell growth or viability.

Cy5-conjugated NB-labeled CAR-T cells were compared with unlabeled control CAR-T cells to assess differentiation, with specific attention to markers such as CD45RA, CCR7, and CD27. Differentiation markers, particularly CD45RA and CCR7, remained unchanged compared to the control, indicating that the labeling process did not alter CAR-T cell differentiation (Fig. S8). Both CD8 and CD4 populations were analyzed *via* flow cytometry, showing no appreciable differences in mean fluorescence intensity (MFI) shifts for any of the biomarkers. This suggests a similar distribution of Effector memory (Ems; CD45RA- and CCR7-), Central Memory (CMs; CD45RA- and CCR7+), and terminal effector memory cells (TEMs; CCR7- and CD45RA+) among the labeled CAR-T cells (Fig. S8). The viability dye 7-AAD was employed to evaluate potential toxicity and the overall viability of NB-labeled cells relative to the controls. These analyses ensured that NB labeling did not adversely affect CAR-T cell differentiation or viability.

Finally, to further assess the functionality of NB-labeled CAR-T cells, we evaluated their activity in a mouse tumor model. NB labeled and unlabeled CD19 CAR-T cells were injected into immunodeficient mice 1 week after RAJI tumor inoculation. Mice that did not receive any CAR-T cells with disseminated RAJI tumors demonstrated rapid tumor progression, as measured by bioluminescence, and began to succumb to the tumor burden after approximately 5 weeks. In contrast, both NB-labeled CAR-T cells and unlabeled CAR-T cells showed similar disease control (Fig. 8e). Our results confirmed no phenotypical or functional differences between the labeled and unlabeled CAR-T cells in terms of proliferation, viability, and cytotoxicity.

Conclusions

Our evaluation of CAR-T cell therapy, enhanced by NB labeling and US imaging, highlights a promising novel methodology for real-time tracking of CAR-T cell distribution and localization both *in vitro* and *in vivo*. This technique has demonstrated efficacy in visualizing CAR-T cell trafficking dynamics, providing insights into therapeutic responses and offering a valuable tool for optimizing treatment strategies. The combination of two FDA-approved techniques highlights the clear translational potential for this procedure to transition into clinical application. *In vitro* studies confirmed the CAR-T cells are labeled with NBs *via* flow cytometry and confocal imaging, demonstrating significant NLC under US imaging with a minimum detection threshold of 10^3 cells per mL, providing a robust method for cell tracking. Additionally, *in vivo* experiments in healthy mice and RAJI tumor models illustrated the feasibility of monitoring CAR-T cell distribution. The initial bolus injection of labeled cells resulted in a distinct increase in NLC followed by gradual signal decay, reflecting cellular redistribution and transit within and around targeted tissues.

These findings underscore the potential of US imaging with NB-labeled CAR-T cells to transform clinical monitoring, offering insights into biodistribution patterns crucial for treatment efficacy assessment. While this study was limited to 75 minutes, it demonstrates that we are capable of real-time tracking of labeled CAR-T cells *in vivo*. However, the longevity of the cellular signal remains a key limitation, longer imaging durations will be assessed moving forward to evaluate the longevity of signal and cell tracking. Extended time points are important because long-term trafficking could reveal how CAR-T cells persist, migrate, and interact with target tissues, which are key indicators of therapeutic success and durability. Future experiments will aim to extend the duration of contrast enhancement in labeled cells and monitor them over longer periods, which could be achieved by adjusting US parameters, such as power, or by using alternative NB formulations with modified shell properties, such as cationic NBs, which may improve cellular uptake and retention compared to anionic NBs. They will also explore alternative tissues and organs to understand the cells' distribution better. Moving from *in vitro* to the clinical application also necessitates optimizing the labeling process, as the costly nature of immunotherapy must ensure high labeling efficiency without compromising efficacy. US NBs are a cost-effective methodology that could be used without hindering the immunotherapy. Additionally, the mechanism of labeling must be investigated to ensure it does not affect the functionality of the cells. Further advancements in this technology could improve personalized therapeutic approaches by optimizing infusion strategies and dosage regimens, thereby enhancing patient outcomes in immunotherapy. While challenges such as signal decay over time and tissue heterogeneity remain, the integration of NB-based US imaging represents a significant step forward in the development of more precise and efficient CAR-T cell therapies for hematological malignancies and potentially beyond, paving the way for future research and clinical applications in cancer treatment. The novelty and importance of being able to track cells continuously after injection, should not be underplayed.

Ethics statement

All animal experiments were performed in compliance with relevant laws and institutional guidelines for the care and use of laboratory animals. All procedures were reviewed and approved by the Institutional Animal Care and Use Committee (IACUC) at Case Western Reserve University under approved protocol number 2014-088. Animal studies were conducted and reported in accordance with the ARRIVE 2.0 guidelines for reporting *in vivo* experiments.

Human peripheral blood samples used in this study were obtained from healthy donors under an Institutional Review Board (IRB), approved protocol at University Hospitals Cleveland Medical Center (IRB protocol number 04-04-22). All donors provided written informed consent prior to sample collection. Samples were de-identified prior to use.

Conflicts of interest

There are no conflicts to declare.

Data availability

Data can be provided upon request by reaching out to the authors.

Supplementary information is available. See https://doi.org/10.1039/d5nh00708a.

Acknowledgements

This work was supported by the National Institutes of Health (R21-CA262736) and the Hematopoietic Biorepository and Cellular Therapy Shared Resource of the Case Comprehensive Cancer Center (P30CA043703). The authors thank T. Kosmides for reviewing the manuscript. Figures were created using BioRender.com.

References

1 A. Mitra, A. Barua, L. Huang, S. Ganguly, Q. Feng and B. He, From bench to bedside: the history and progress of CAR T cell therapy, *Front. Immunol.*, 2023, **14**, DOI: 10.3389/FIMMU.2023.1188049.

2 M. Sheykhhasan, A. Ahmadieh-Yazdi and R. Vicidomini, *et al.*, CAR T therapies in multiple myeloma: unleashing the future, *Cancer Gene Ther.*, 2024, **31**(5), 667–686, DOI: 10.1038/s41417-024-00750-2.

3 S. M. Albelda, CAR T cell therapy for patients with solid tumours: key lessons to learn and unlearn, *Nat. Rev. Clin. Oncol.*, 2023, **21**(1), 47–66, DOI: 10.1038/s41571-023-00832-4.

4 R. C. Sterner and R. M. Sterner, CAR-T cell therapy: current limitations and potential strategies, *Blood Cancer J.*, 2021, **11**, 69, DOI: 10.1038/s41408-021-00459-7.
5 J. Franklin, P. Pophali, Z. Jackson, D. Wald and D. Avigan, CAR-T cell therapy, in *Molecular Hematology*, Wiley, 2024, 369–396, DOI: 10.1002/9781394180486.ch25.
6 C. Y. Jiang, Z. Niu and M. D. Green, *et al.*, It's not ''just a tube of blood'': principles of protocol development, sample collection, staffing and budget considerations for blood-based biomarkers in immunotherapy studies, *J. Immunother. Cancer*, 2021, **9**, 3212, DOI: 10.1136/jitc-2021-003212.
7 Q. Li, D. Hu, D. Gao, G. Gao, C. Zhang and Z. Sheng, Optical imaging of in vivo adoptive T-cell therapy: State of the art and challenges, *iRadiology*, 2023, **1**(3), 225–235, DOI: 10.1002/IRD3.28.
8 X. Y. Wang, Y. Wang, Q. Wu, J. J. Liu, Y. Liu, D. H. Pan, W. Qi, L. Z. Wang, J. J. Yan, Y. P. Xu and G. J. Wang, Feasibility study of 68Ga-labeled CAR T cells for in vivo tracking using micropositron emission tomography imaging, *Acta Pharmacol. Sin.*, 2021, **42**(5), 824–831, DOI: 10.1038/s41401-020-00511-5.
9 V. P. Dubois, O. C. Sehl, P. J. Foster and J. A. Ronald, Visualizing CAR-T cell Immunotherapy Using 3 Tesla Fluorine-19 MRI, *Mol. Imaging Biol.*, 2022, **2**, 298–308, DOI: 10.1007/s11307-021-01672-3.
10 Y. Su, J. R. Walker and Y. Park, *et al.*, Novel NanoLuc substrates enable bright two-population bioluminescence imaging in animals, *Nat. Methods*, 2020, **17**(8), 852–860, DOI: 10.1038/s41592-020-0889-6.
11 R. Sakemura, I. Can, E. L. Siegler and S. S. Kenderian, In vivo CART cell imaging: Paving the way for success in CART cell therapy, *Mol. Ther. Oncolytics*, 2021, **20**, 625–633, DOI: 10.1016/j.omto.2021.03.003.
12 M. A. Sellmyer, S. A. Richman and K. Lohith, *et al.*, Imaging CAR T Cell Trafficking with eDHFR as a PET Reporter Gene, *Mol. Ther.*, 2020, **28**(1), 42–51, DOI: 10.1016/j.ymthe.2019.10.007.
13 U. Himmelreich and M. Hoehn, Stem cell labeling for magnetic resonance imaging, *Minim. Invasiv. Ther.*, 2008, **17**(2), 132–142, DOI: 10.1080/13645700801969873.
14 Z. Zhang, N. Mascheri, R. Dharmakumar and D. Li, Cellular magnetic resonance imaging: potential for use in assessing aspects of cardiovascular disease, *Cytotherapy*, 2008, **10**(6), 575, DOI: 10.1080/14653240802165699.
15 A. A. Exner and M. C. Kolios, Bursting Microbubbles: How Nanobubble Contrast Agents Can Enable the Future of Medical Ultrasound Molecular Imaging and Image-Guided Therapy, *Curr. Opin. Colloid Interface Sci.*, 2021, **54**, DOI: 10.1016/j.cocis.2021.101463.
16 M. Rodriguez-Porcel, O. Gheysens, I. Y. Chen, J. C. Wu and S. S. Gambhir, Image-Guided Cardiac Cell Delivery Using High-Resolution Small-Animal Ultrasound, *Mol. Ther.*, 2005, **12**(6), 1142–1147, DOI: 10.1016/j.ymthe.2005.07.532.
17 B. H. Grubbs, M. Millan Ching, K. R. Parducho, R. H. Chmait and T. Miki, Ultrasound-guided in utero transplantation of placental stem cells into the liver of Crigler-Najjar Syndrome (CNS) model rat, *Transplantation*, 2019, **103**(7), e182–e187, DOI: 10.1097/TP.0000000000002735.
18 F. Chen and JV. Jokerst, Stem Cell Tracking with Nanoparticle-Based Ultrasound Contrast Agents, *Methods Mol. Biol.*, 2020, **2126**, 141–153, DOI: 10.1007/978-1-0716-0364-2_13.
19 W. Cui, S. Tavri and M. J. Benchimol, *et al.*, Neural progenitor cells labeling with microbubble contrast agent for ultrasound imaging invivo, *Biomaterials*, 2013, **34**(21), 4926–4935, DOI: 10.1016/j.biomaterials.2013.03.020.
20 Y. Jiang, X. Hou, X. Zhao, J. Jing and L. Sun, Tracking adoptive natural killer cells via ultrasound imaging assisted with nanobubbles, *Acta Biomater.*, 2023, **169**, 542–555, DOI: 10.1016/j.actbio.2023.07.058.
21 Y. Huang, Z. Yin and R. Xu, *et al.*, Gas Vesicle-Assisted Ultrasound Imaging for Effective Anti-Tumour CAR-T Cell Immunotherapy Efficacy in Mice Model, *Int. J. Nanomed.*, 2025, **20**, 4849–4862, DOI: 10.2147/IJN.S508846.
22 S. Hernot and A. L. Klibanov, Microbubbles in ultrasound-triggered drug and gene delivery, *Adv. Drug Delivery Rev.*, 2008, **60**(10), 1153–1166, DOI: 10.1016/j.addr.2008.03.005.
23 Y. Endo-Takahashi and Y. Negishi, Microbubbles and Nanobubbles with Ultrasound for Systemic Gene Delivery, *Pharmaceutics*, 2020, **964**, DOI: 10.3390/pharmaceutics12100964.
24 J. E. Lemaster, F. Chen, T. Kim, A. Hariri and J. V. Jokerst, Development of a Trimodal Contrast Agent for Acoustic and Magnetic Particle Imaging of Stem Cells, *ACS Appl. Nano Mater.*, 2018, **1**(3), 1321–1331, DOI: 10.1021/acsanm.8b00063.
25 R. H. Perera, A. de Leon and X. Wang, *et al.*, Real time ultrasound molecular imaging of prostate cancer with PSMA-targeted nanobubbles, *Nanomedicine*, 2020, **28**, 102213, DOI: 10.1016/j.nano.2020.102213.
26 R. H. Perera, E. Abenojar and P. Nittayacharn, *et al.*, Intracellular vesicle entrapment of nanobubble ultrasound contrast agents targeted to PSMA promotes prolonged enhancement and stability in vivo and in vitro, *Nanotheranostics*, 2022, **6**(3), 270–285, DOI: 10.7150/ntno.64735.
27 S. Capolla, M. Argenziano and S. Bozzer, *et al.*, Targeted chitosan nanobubbles as a strategy to down-regulate microRNA-17 into B-cell lymphoma models, *Front. Immunol.*, 2023, **14**, DOI: 10.3389/FIMMU.2023.1200310.
28 S. Ghassemi, S. Nunez-Cruz and O. RS, *et al.*, Reducing Ex Vivo Culture Improves the Antileukemic Activity of Chimeric Antigen Receptor (CAR) T Cells HHS Public Access. Cancer, *Immunol. Res.*, 2018, **6**(9), 1100–1109, DOI: 10.1158/2326-6066.CIR-17-0405.
29 T. Xu, F. Yang and R. Liu, *et al.*, Evaluating the Impact of Cryopreservation of PBMCs on CAR-T Therapy Efficacy and Safety in DLBCL Patients: An Informative Approach to Optimize Manufacturing Strategies, *Blood*, 2023, **142**(1), 3513, DOI: 10.1182/BLOOD-2023-185590.
30 A. de Leon, R. Perera, C. Hernandez, M. Cooley, O. Jung, S. Jeganathan, E. Abenojar, G. Fishbein, A. Sojahrood, C. Emerson, P Stewart, M. Kolios and A. Exner, Contrast enhanced ultrasound imaging by nature-inspired ultrastable echogenic nanobubbles, *Nanoscale*, 2019, **11**, DOI: 10.1039/c9nr04828f.
31 D. Omata, T. Maruyama and J. Unga, *et al.*, Effects of encapsulated gas on stability of lipid-based microbubbles

and ultrasound-triggered drug delivery, *J. Controlled Release*, 2019, **311–312**, 65–73, DOI: 10.1016/j.jconrel.2019.08.023.

32 J. E. Chomas, P. Dayton and J. Allen, *et al.*, Mechanisms of Contrast Agent Destruction, *IEEE Trans. Ultrason. Eng.*, 2001, **48**(1), 232–248, DOI: 10.1109/58.896136.

33 D. Wegierak, M. B. Cooley and R. Perera, *et al.*, Decorrelation Time Mapping as an Analysis Tool for Nanobubble-Based Contrast Enhanced Ultrasound Imaging, *IEEE Trans. Med. Imaging*, 2024, **43**(6), DOI: 10.1109/TMI.2024.3364076.

34 C. Theodoropoulos and S. Foster, Andrew Needles VisualSonics White Paper: Nonlinear Contrast Agent Imaging with a High Frequency Linear Array Based System VSI White Paper: Nonlinear Contrast Agent Imaging with a High Frequency Linear Array Based System; 2009.

35 Z. Ying, T. He and X. Wang, *et al.*, Distribution of chimeric antigen receptor-modified T cells against CD19 in B-cell malignancies, *BMC Cancer*, 2021, **21**(1), DOI: 10.1186/s12885-021-07934-1.

36 H. Wen, Y. Huang, T. Hou, J. Wang and Y. Huo, Determination of the biodistribution of chimeric antigen receptor-modified T cells against CD19 in NSG mice, in *Methods in Cell Biology*, Academic Press Inc., 2022, vol. 167, pp. 15–37, DOI: 10.1016/bs.mcb.2021.08.003.

37 P. Bankhead, M. B. Loughrey and J. A. Fernández, *et al.*, QuPath: Open source software for digital pathology image analysis, *Sci. Rep.*, 2017, **7**(1), DOI: 10.1038/s41598-017-17204-5.

38 K. Fousek, J. Watanabe and S. K. Joseph, *et al.*, CAR T-cells that target acute B-lineage leukemia irrespective of CD19 expression, *Leukemia*, 2020, **35**, 1, DOI: 10.1038/s41375-020-0792-2.

39 D. Lainšček, A. Golob-Urbanc, V. Mikolič, J. Pantović-Žalig, Š. Malenšek and R. Jerala, Regulation of CD19 CAR-T cell activation based on an engineered downstream transcription factor, *Mol. Ther. Oncolytics*, 2023, **29**, 77, DOI: 10.1016/J.OMTO.2023.04.005.

40 S. Shahabuddin Hoseini, M. Espinosa-Cotton, G. H. Fen and N. K. V. Cheung, Overcoming leukemia heterogeneity by combining T cell engaging bispecific antibodies, *J. Immunother. Cancer*, 2020, **8**, 1626, DOI: 10.1136/jitc-2020-001626.

41 I. Dagogo-Jack and A. T. Shaw, Tumour heterogeneity and resistance to cancer therapies, *Nat. Rev. Clin. Oncol.*, 2017, **15**(2), 81–94, DOI: 10.1038/nrclinonc.2017.166.

42 A. M. Alviano, M. Biondi, E. Grassenis, A. Biondi, M. Serafini and S. Tettamanti, Fully equipped CARs to address tumor heterogeneity, enhance safety, and improve the functionality of cellular immunotherapies, *Front. Immunol.*, 2024, **15**, 1407992, DOI: 10.3389/FIMMU.2024.1407992/BIBTEX.